Damage and fracture of polyvinylidene fluoride (PVDF) at 20°C: Experiments and modelling

Mélanie Challier, Jacques Besson, Lucien Laiarinandrasana, Roland Piques

Damage and fracture of polyvinylidene fluoride (PVDF) at 20 °C: Experiments and modelling

Mélanie Challier *, Jacques Besson, Lucien Laiarinandrasana, Roland Piques

Centre P.M. Fourt, Ecole des Mines de Paris, UMR CNRS 7633, BP 87, 91003 Evry, France

Flexible oil pipelines are multilayered structures used for the transport of crude oil or natural gas from the seabed to the surface in offshore oil fields. Because of severe service conditions, composite structures made of metallic and poly-meric layers must be used. PVDF is a good candidate as it accommodates tensile and flexural deformations and guar-antees water tightness. The present paper focuses on the mechanical properties of PVDF at 20 °C. Several specimens with different geometries were tested: smooth specimens, notched specimens and cracked specimens under tension and bending. Fracture surfaces were examined to determine fracture mechanisms. Based on mechanical testing and microscopic observations, a modified Gurson–Tvergaard–Needleman model for semi-crystalline polymers is proposed. The model allows both the non-linear behavior and the cracking of polymer structures to be represented.

Keywords: Polymers; Ductile fracture; Scanning electron microscopy; Damage; Finite element analysis

1. Introduction

Polyvinylidene fluoride (PVDF) is a semi-crystalline polymer that has been widely studied for its piezo-electric properties [1,2], due to its polar β phase. Nevertheless, the apolar phase α is also studied for struc-tural applications, because it exhibits good mechanical properties and chemical resistance [3]. Mechanical properties of PVDF have been already studied by many authors, who analysed the macroscopic tensile and

* Corresponding author. Tel.: +33 1 60 76 30 64; fax: +33 1 60 76 31 60.
E-mail address: lucien.laiarinandrasana@ensmp.fr (L. Laiarinandrasana).

creep behavior over several strain rate decades, and over a large range of temperatures [4,5]. During viscoplastic deformation, the material whitens after the onset of necking due to nucleation and growth of voids, as evidenced using small and large angle X-ray diffraction [3]. In this study, an α-PVDF grade used for offshore applications is analysed at 20 °C with respect to viscoplastic and damage behavior. Notched specimens and cracked specimens were used in order to investigate damage development over a wide range of loading conditions. A numerical simulation of these tests is performed using the Gurson model [6] which was adapted to the present material.

2. Materials and experimental procedures

2.1. Materials

The material of the study was provided by ARKEMA. It is used in multilayered offshore risers. In order to prevent from any kind of ageing effect, the material was extruded without plasticizer. Hence it differs from the standard industrial grade. The lack of plasticizer leads to a difficult extrusion, which creates a significant porosity. The initial defect population was estimated by microscopic examination followed by image analysis, of a PVDF sample broken in liquid nitrogen. The porosity is equal to 10%. It consists of 1 μm diameter voids which are always observed in bulk PVDF and that are created during crystallisation and extrusion [4]. A second, much smaller (0.1 μm) population is also observed in the investigated material. The unplasticized PVDF can exhibit brittle failure at 20 °C which is not observed in industrial PVDF. Results reported in this study give consequently a pessimistic evaluation of the rupture properties.

2.2. Experimental procedures

Tensile and flexural tests were made on different geometries. Smooth specimens were machined from PVDF 6 mm extruded sheets (ASTM D638 M1) with a gauge length of 100 mm and a cross section equal to $6 \times 8\ \text{mm}^2$. All tensile tests were carried out using an Inströn testing machine, at constant crosshead speed, ranging from 0.015 to 15 mm s^{-1} (corresponding to a strain rate between 1.5×10^{-4} and $1.5 \times 10^{-1}\ \text{s}^{-1}$). A strain gage extensometer is also used, its gauge length is 25 mm.

Circumferentially notched round bars (CNRB) were also tested, in tension, and tests have been performed using three notch radii: CNRB 4: $R = 4$ mm, CNRB 1.6: $R = 1.6$ mm, CNRB 0.8: $R = 0.8$ mm. All specimens have a 65-mm length, the diameter in the minimal cross section is 4 mm, and the maximum diameter is 7.2 mm. A strain gage is positioned at the notch tip in order to record the decrease of the minimum diameter. The crosshead displacement is also measured. Tests have been carried out by controlling either the crosshead displacement (0.15 mm s^{-1}), or the diameter reduction (2.5×10^{-3} mm s^{-1}). Double edge notched specimens were tested in tension (DENT). They were machined from PVDF 12 mm thick extruded sheets (ASTM D638 M1). The length is 100 mm, the width (W) is 6 mm and the thickness is 12 mm. Various crack length (a) width ratios (a/W) are used ranging from 0.1 to 0.5. The cracks are made with a cutter blade. Special attention is paid to guarantee alignment of both cracks. Initial crack lengths are measured from the fracture surfaces using an optical microscope. DENT tests are carried out at constant crosshead speed (0.15 mm s^{-1}), and a gage extensometer (gage length: 7 mm) is used to follow the crack opening displacement (COD).

Single edge notched specimens (SENB) were tested in three point bending at a constant displacement rate (0.15 mm s^{-1}) using an Inströn machine. Specimens were tested using a span-to-specimen width ratio, S/W, of 4:1. Width (W) and thickness (B) are respectively 14 mm and 7 mm, and the a/W ratio was 0.5. Displacement and load are monitored together with the crack opening displacement measured using a MTS extensometer.

3. Results of mechanical testing

3.1. Tensile tests on smooth and CNRB specimens

Nominal stress–strain curves on smooth specimens are shown in Fig. 1 for the different displacement rates, exhibiting a strong influence of the strain rate on the non-linear behavior. The maximum load is increased by 22% for strain rates varying between 1.5×10^{-4} and 1.5×10^{-1} s^{-1} whereas the nominal strain at fracture is decreased by 40%. This decrease is likely related to material softening caused by temperature elevation [7].

Engineering thermoplastics are significantly notch-sensitive. They exhibit a brittle mode of failure in notched specimens, which generate a state of sufficiently large hydrostatic tension ahead of the notch [8,9]. This stress state also promotes void growth. Decreasing the notch radius leads to an increase of the maximum load as the stress triaxiality ratio (τ) is increased [10].

Typical results on CNRB are shown in Fig. 2 for the three notch radii, where the load is plotted versus radial displacement. As expected, fracture occurs sooner with small radii. Large plastic deformation is obtained for CNRB 4. In all cases, a maximum load is observed followed by a post-yield softening and a load plateau before final rupture. Note that this last effect is not monitored on smooth specimens as necking occurs after the maximum load so the displacement measured by the longitudinal extensometer is no longer representative of the deformation in the neck region. As the cross section diminishes, the load plateau actually corresponds to a strain hardening phase.

This two stage deformation process can qualitatively be related to the microscopic deformation mechanisms of the porous semi-crystalline polymer. First, elongation of amorphous tie chains followed by slip and tilting of crystalline lamellar chains, and orientation of crystal blocks occur [11]. This corresponds to moderate hardening rates. Then, once the spherulite microstructure has been destroyed and transformed into a fibrillar microstructure, deformation occurs by destruction of the lamellar morphology. This last deformation process induces a strong strain hardening. Indeed the hardening mechanisms are coupled with void growth induced softening (see below).

Results obtained on CNRB 4 and CNRB 1.6 also indicate an increase of maximum load. But no similar effect is obtained between CNRB 1.6 and CNRB 0.8. The maximum load reaches a limit value for radii smaller than 1.6 mm. In order to check this effect, similar tests were carried out on the same geometry under

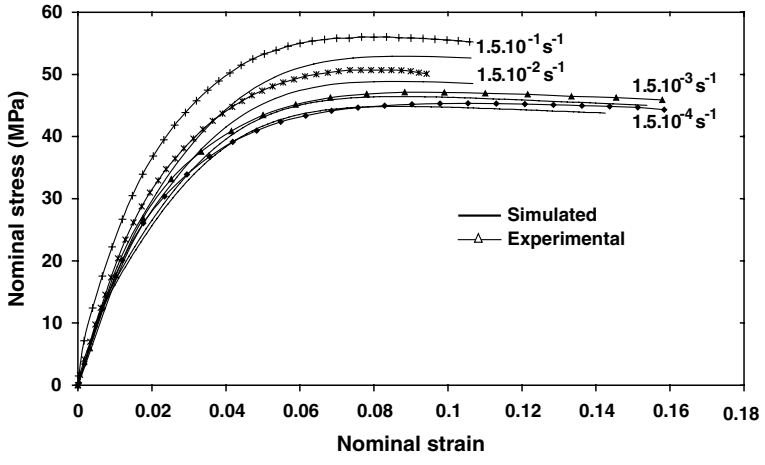

Fig. 1. Simulated and experimental nominal stress versus nominal strain, on smooth specimens, for different strain rates.

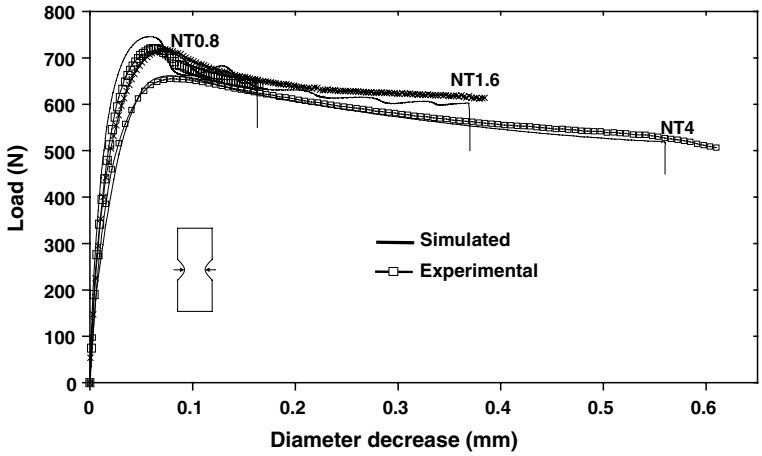

Fig. 2. Load versus diameter decrease curves for NT 0.8, NT 1.6 and NT 4 notched specimens at a radial decrease rate equal to 2.5×10^{-3} mm s^{-1}. (NT*xx* indicates: Notched specimen Tensile with *xx* mm initial radius).

similar conditions but with a 0.15 mm radius (CNRB 0.15). The same maximum load was obtained. Ductile initiation followed by brittle fracture are observed whereas the other specimens failure mode was ductile. Similar results have been reported in bending on other engineering thermoplastics [8,12,13]. It is shown that fracture becomes brittle when the notch radius is decreased as a constrained plastic zone is formed at the notch root where hydrostatic stresses are high leading to brittle fracture. In conclusion, all results clearly indicate that brittleness is favored by high triaxiality ratios.

3.2. Tensile and flexural tests on cracked specimens

Tensile tests on DENT are carried out to induce more severe loading conditions compared to CNRB specimens. A constrained plastic zone is confined at the crack tip. Fig. 3 displays the load versus COD,

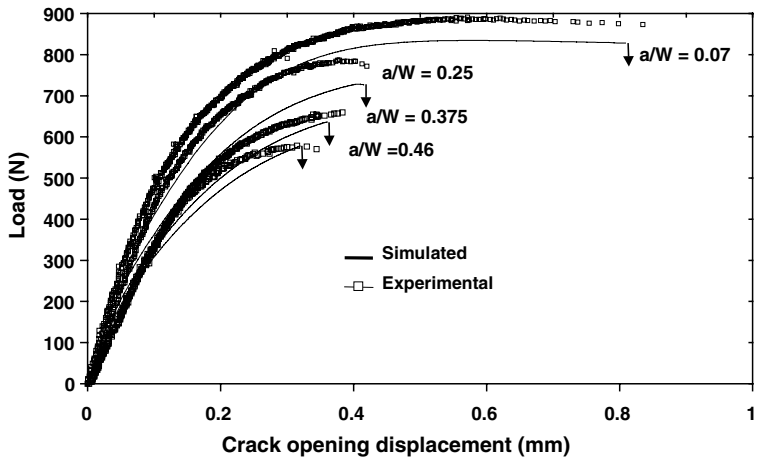

Fig. 3. Simulated and experimental load–COD curves for DENT using 3D calculations at a displacement rate of 0.15 mm s^{-1} for different *a*/*W* ratios.

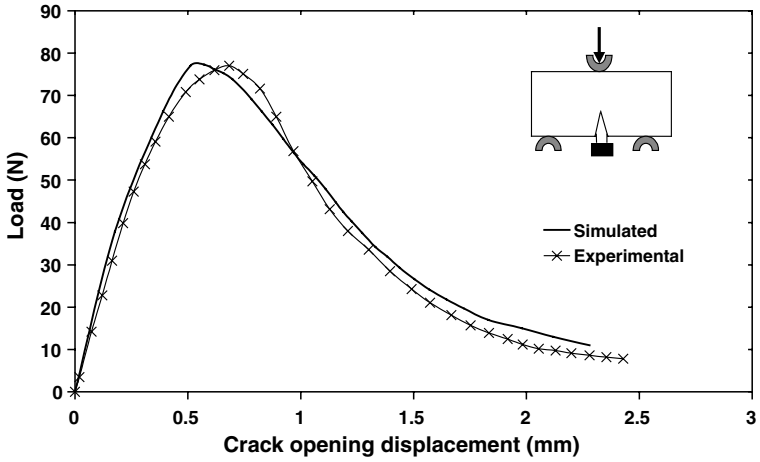

Fig. 4. Simulated and experimental load–crack opening displacement curves for SENB in 3D calculations, (load line displacement rate 0.15 mm s^{-1}).

for a/W ratios between 0.07 and 0.46. In all cases, fracture is unstable. On the other hand, flexural tests on SENB indicate that crack propagation is stable during the test at 20 °C, Fig. 4.

Differences between cracked specimen fracture under tension and under bending have been explained by Paris et al. [14]. They proposed an approach to the stability analysis of crack growth based on the J–Δa curve. They established that stable or unstable propagation is a function of the specimen length; this dependence is strong for DENT. This geometry exhibits higher risk of unstable fracture, especially if the specimen is long. Conversely, they indicated that the stability of SENB specimens increases as the crack propagates [15].

4. Microscopic observations

Fracture surfaces of notched specimens have been observed by scanning electron microscopy (SEM). Interrupted CRNB tests have been carried out to highlight damage development and localisation. Tensile tests were stopped just prior to fracture. Then, the specimens were microtomed along the tensile direction. Optical observations of 2-μm thick lamellae and SEM observations of longitudinal cross sections indicated that for the two smaller radii, a localised damage band, containing many cavities, is observed in the minimal cross section, Fig. 5a. Crazing is not observed and voids are larger at the specimen centre, where stress triaxiality ratio is high. The damage band width decreases for smaller radii.

Fracture surfaces observed in SEM indicate an initiation site located at the centre of the minimum cross section. The macroscopic crack is initiated on a cavity or on a particle, Fig. 5b. EDX analysis revealed these particles are composed of potassium salt or calcium salt. Radial propagation is characterised by many large cavities. Diameter of voids diminishes with propagation, and striations could also be observed at the end of ductile propagation close to specimen edges, Fig. 5c.

Optical observations carried out during the DENT test show that the white zone is located at the crack tip indicating that the deformation and damage remain confined. Blunting up to 60 μm was observed prior to crack initiation in a test performed in situ in the SEM chamber. Crack initiation is always ductile and quickly followed by unstable brittle fracture, Fig. 6. Crack propagation is always larger at the centre of the specimen (tunnelling effect) where plane strain conditions (high stress triaxiality) prevail. Plane stress

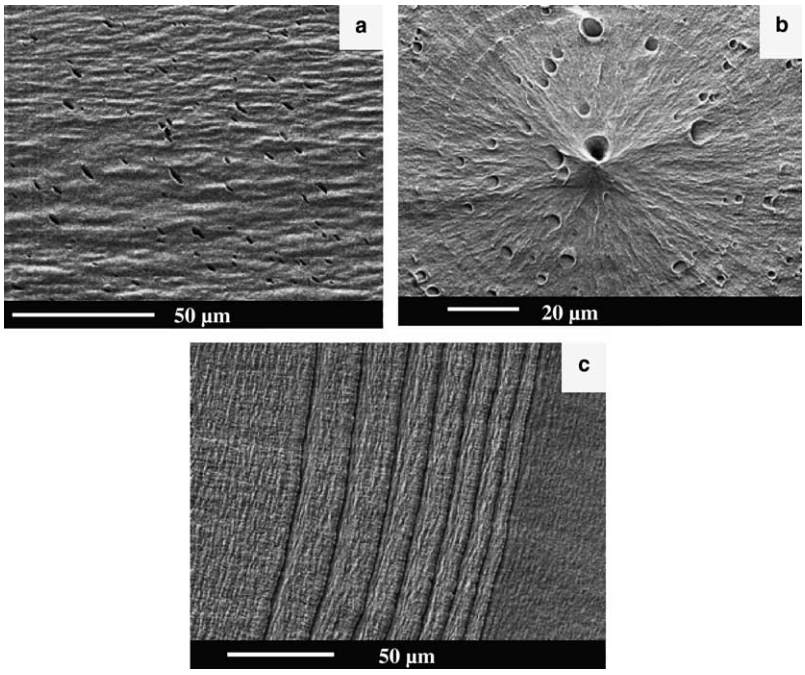

Fig. 5. SEM observations of (a) microtomed longitudinal section area of interrupted CNRB 0.8 test, (b) initiation site on CNRB 0.8 fracture surface, (c) striations observed during propagation on CNRB 0.8 fracture surface.

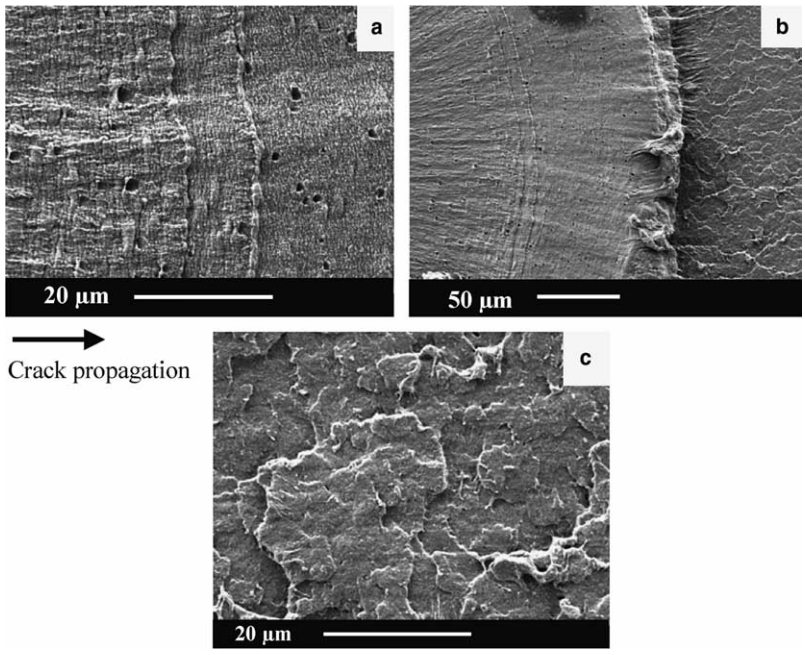

Fig. 6. SEM observations of (a) ductile propagation on DENT, (b) ductile–brittle transition area on DENT, (c) brittle surface on DENT.

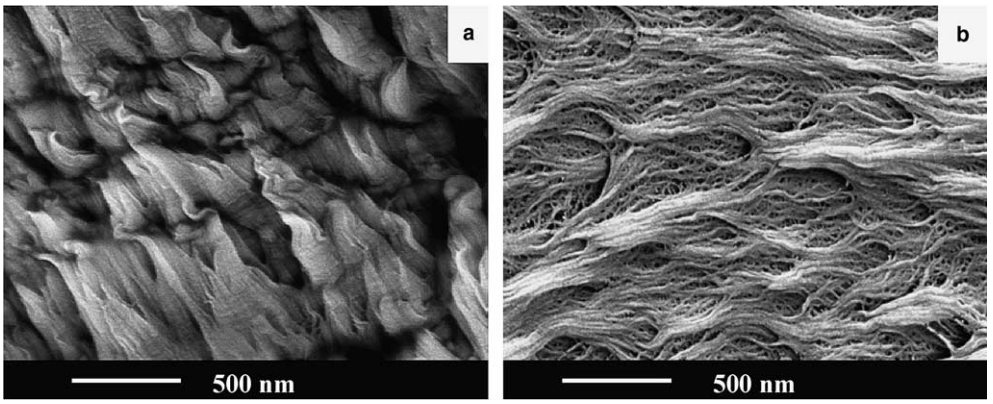

Fig. 7. SEM observations of fracture surfaces: (a) smooth tensile specimen: fibrillar stretching, (b) CNRB 0.8: void growth and coalescence.

conditions (low stress triaxiality) are met at the free surfaces. The percentage of brittle zone on the fracture surface was evaluated for different a/W ratios. It is a slightly increasing function of the initial crack length (from 70% for $a/W = 0.07$–80% for $a/W = 0.46$). This trend is related to the confinement of the crack tip plastic zone which is more pronounced for the deep cracks; this leads to higher stress triaxialities which favor brittle fracture [16]. Striations are also observed close to the ductile–brittle transition zone.

From the study of CNRB and DENT specimens, it is concluded that macroscopic crack initiation is always ductile followed by a stable ductile crack advance. As the crack grows, it becomes unstable so that quasi-static loading conditions do not prevail any longer. Under dynamic conditions, unloading of the crack tip can occur leading to crack arrests which create striation marks similar to what is observed under fatigue loading [17]. The observed distance between the striations (10–20 μm) is consistent with observations on fatigued polymers [17]. As the crack speed further increases, stresses are increased, due to the strain rate dependence of the material, so that brittle fracture is triggered.

Brittle fracture was not observed in three point bending. Observation of the fracture surface showed that the crack had blunted to an estimated radius of about 100 μm before initiation. Then, subsequent patterns revealed a stable propagation without striations, but with many cavities.

Ductile propagation was observed on the different specimen fracture surfaces under tension and under bending. A comparison can be made as a function of the stress triaxiality ratio $\tau = \sigma_m/\sigma_{eq}$ where σ_m and σ_{eq} are respectively the mean stress and the equivalent stress. Ductile fracture of smooth specimens (low τ) are characterised by material stretching (Fig. 7a), whereas for CNRB 08 (high τ), many large cavities are observed on fracture surface (Fig. 7b). On SENB fracture surfaces, both cavities and material stretching can be observed. This indicates that final rupture can be controlled by two different mechanisms: (i) fibril stretching up to their limit elongation for low triaxialities, (ii) void coalescence for high triaxialities [18].

5. Damage quantification on notched specimens

As the initial material porosity is high, significant volume variations can be expected during testing. Video acquisition followed by image processing was used to follow the volume variation. This technique has already been used for tensile tests on smooth specimens [19,20]. In this study, it was also applied to notched specimens. As shown in Fig. 8, the outer surface located on both sides of the minimum cross section is painted in black to track its evolution using the video acquisition system. The height of the

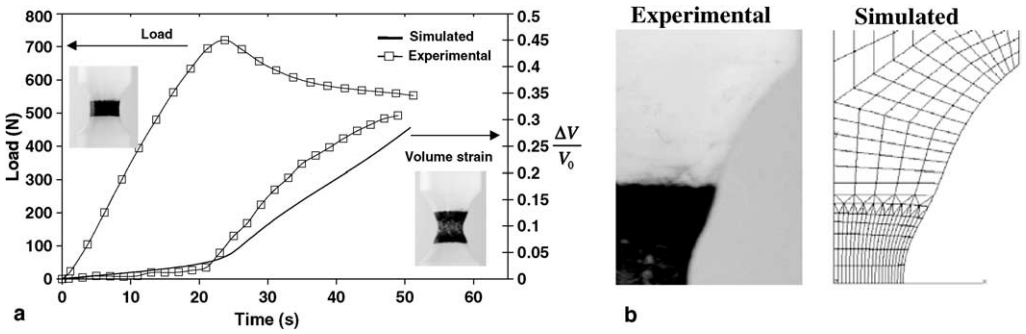

Fig. 8. (a) Force and volume variation for a tensile test performed at 0.05 mm s^{-1} on a CNRB 4, (b) experimental and simulated deformation of the notch region.

painted zone is chosen to match the extension of the whitened (i.e. damaged) region. The volume change is then computed for each load step assuming that initially straight cross sections remains straight. This leads to a slight error on the calculated volume change. Tests were conducted on CNRB 4 and CNRB 0.8 samples at a crosshead speed equal to 0.05 mm s^{-1}. Results are shown in Fig. 8a for a CNRB 4 where the load and the relative volume change $\Delta V/V_0$ are plotted against time. Volume starts to strongly increase slightly before the maximum load, which corresponds to the onset of whitening. For high levels of deformation, the rate of volume change decreases; at this stage void growth is probably limited by fibrils stretching. Similar conclusions are drawn from tests performed on CNRB 0.8 specimens. As these measurements involve both effects related to the material behavior and structural effects, they cannot be directly interpreted. However, they can be used to adjust the parameters of the constitutive models used to represent deformation and damage behavior (see below).

6. Modelling

6.1. Model

The model is based on Gurson's yield function [6], extended by Needleman and Tvergaard [21,22], and Besson et al. [23] to incorporate isotropic hardening, strain rates effect and coalescence. An effective stress, σ^* depending on damage is defined by

$$\Phi(\sigma, \sigma^*, f) = \frac{\sigma_{\mathrm{eq}}^2}{\sigma^{*2}} + 2q_1 \cdot f \cdot \cosh\left(\frac{q_2\sigma_{\mathrm{kk}}}{2\sigma^*}\right) - 1 - q_1^2 f^{2^{\mathrm{def}\cdot\sigma^*}} = 0 \tag{1}$$

σ_{eq} is the von Mises stress, and σ_{kk} the trace of the stress tensor. f is the porosity, q_1 and q_2 are model parameters that were introduced to improve the model predictions for periodic arrays of cylindrical and spherical voids. The yield surface is now expressed as $\Phi = \sigma^* - R$ where R is the flow stress of the matrix material. Note that hardening was supposed to be isotropic as the study is only concerned with monotonic loadings. The viscoplastic strain rate tensor, $\underline{\dot{\varepsilon}}_{vp}$, is given by the normality rule as

$$\underline{\dot{\varepsilon}}_{vp} = (1-f)\dot{p}\frac{\partial \Phi}{\partial \underline{\sigma}} \tag{2}$$

so that $(1-f)\dot{p}\sigma^* = \underline{\sigma} : \underline{\dot{\varepsilon}}_{vp} \cdot \dot{p}$ is given using the matrix viscoplastic law which will be expressed as a Norton law: $\dot{p} = (\frac{\Phi}{K})^n$. The evolution of porosity is expressed using mass conservation $\dot{f} = (1-f)\mathrm{trace}(\underline{\dot{\varepsilon}}_{vp})$.

Several parameters need to be identified. The first set is related to the polymer matrix behavior: R, K, n. A second set is used to describe damage evolution: q_1, q_2. As the initial porosity is high, all these parameters need to be adjusted simultaneously. This identification was performed using tensile tests on smooth specimens, Fig. 1, and tests on CNRB specimens using both the force–displacement curves (Section 3.1) and volume variation measurements (Section 5). The model is validated by simulating the mechanical response of DENT and SENB specimens.

Poisson's ratio, v was fixed at 0.38, and the Young's modulus, $E = 2$ GPa, was identified together with the other parameters. The material flow stress is expressed as

$$R = R_0 + Q(1 - \exp(-bp)) + A(\exp(Bp) - 1) \tag{3}$$

As $R(p = 0) = 10$ MPa, the material almost immediately yields. The first term ($Q(1 - \exp(-bp))$) describes the initial hardening stage, i.e. the deformation of the amorphous phase. The second term ($A(\exp(Bp) - 1)$) allows the simulation of the large stretching of the fibrils, which leads to a rapidly increasing stress.

6.2. Model identification

To simulate the post-yield softening (Figs. 2 and 8a), it is necessary to use large values of q_2. As the material deforms, elongated cavities are formed between the fibrils so that their growth rate is decreased [4]. This corresponds to the evolution of the volume change for large deformation reported in Section 5. Consequently, q_2 was expressed as a function of the maximum principal plastic strain p_1. Note that using a large value for q_1, did allow a good fit of both the load–displacement curves (Fig. 2) and the volume variation (Fig. 8a) to be obtained.

Optimized parameters are gathered in Table 1. Comparisons of experimental and adjusted curves are shown in Figs. 1–4 and 8. Fig. 8b compares the experimental and computed deformed shapes of a CNRB 4 sample just before fracture. A good agreement is obtained. In particular, denotching is followed by renotching. From the FE results it can be observed that the originally straight mesh remains straight so that the computed volume variation (Section 5) corresponds to the actual one. The load plateau observed after the post-yield softening is the result of two opposite effects: (i) void growth (i.e. strong softening), (ii) chain elongation (i.e. strong hardening). Note that fitting the hardening and damage parameters without considering the volume change data leads to a much lower value of q_2, and a less pronounced strain hardening. However, the actual volume change is in that case strongly underestimated.

Table 1
Optimized matrix behavior and damage parameters

Matrix behavior parameters
Elasticity $E = 2$ GPa, $v = 0.38$
Strain rate effect $n = 5$, $K = 20$ MPa, $Q = 40$ MPa, $b = 75$
Flow stress $A = 11$ MPa, $B = 1.6$
Damage parameters
Void growth $f_0 = 0.1$, $q_1 = 0.8$, $q_2 = \begin{cases} 1.55 & \text{if } p_1 < 0.2 \\ 1 + \exp(-3p) & \text{if } p_1 \geqslant 0.2 \end{cases}$
Final rupture $f_c = 0.65$ or $p_c = 1.1$

To represent the two failure criteria, final fracture is assumed to occur when the porosity reaches a critical value f_c or when the principal maximum plastic strain reaches a critical value p_c. The material is considered as broken when either of these conditions is met. At high stress triaxiality, void growth is promoted so that the porosity reaches f_c for values of the plastic strain less than p_c. At low stress triaxiality, the strain based failure criterion is met first. p_c was adjusted on smooth and CNRB 4 specimens in order to fit the minimum diameter at failure. f_c was adjusted in a similar way on CNRB 0.8 and CNRB 0.15 specimens.

6.3. Model validation

DENT and SENB specimens are simulated to validate the model. To represent the tunnelling effect, it is necessary to use a 3D mesh. Due to the symmetries, only one eighth of a DENT specimen is meshed, and only one quarter of a SENB specimen. Calculations were performed using quadratic 20-node bricks with reduced integration (i.e. 8 Gauss points). Due to the softening characters of the constitutive equations, FE results strongly depend on the mesh size [8]. It is therefore necessary to use a constant mesh size to discretise zones where the crack propagates. In this study, the element height in the direction perpendicular to the crack propagation plane is equal to 50 μm. This length was chosen as it approximately corresponds to the width of the highly damaged localisation band observed in Fig. 5a. Using this mesh size, it was possible to accurately model all the specimens so that fitting of the mesh size was not necessary [24]. Simulated load/crack-mouth opening curves for DENT are compared to experimental data in Fig. 4 showing a good agreement, for the different values of the a/W ratios. Simulation indicates that the macroscopic crack is initiated at the maximum load. As experimentally observed, stable crack growth is simulated for a crack advance between $0.2(W-a)$ and $0.3(W-a)$. At this point, the load rapidly decreases which corresponds to the experimentally observed onset of instability. The model can no longer be applied as it does not account for: (i) dynamic effects, (ii) adiabatic heating, (iii) ductile to brittle failure transition. For SENB specimens, crack propagation is initiated at maximum load.

The failure mechanism can be deduced from the numerical simulations. For CNRB 1.6, SENB and DENT specimens, both failure criteria are met almost simultaneously. This result is corroborated by SEM observations of the fracture surfaces which exhibit an appearance intermediate between pure stretching (Fig. 7a) and pure coalescence (Fig. 7b). On CNRB 0.15, failure is controlled by coalescence as observed experimentally.

Simulated crack extension for SENB and DENT specimens is plotted as a function of the imposed displacement in Figs. 9 and 10. As observed experimentally, propagation is stable for SENB specimens. For DENT, the crack becomes unstable after stable extensions between 400 and 800 μm depending on the a/W

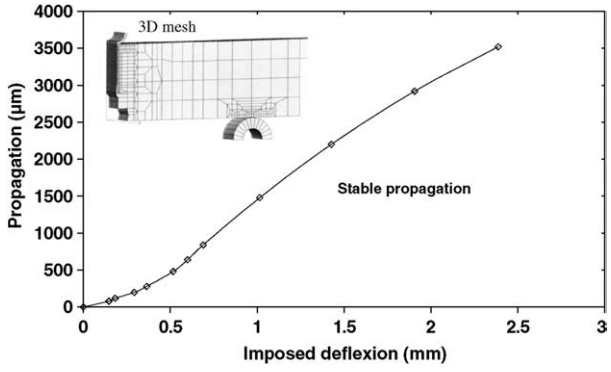

Fig. 9. Simulated crack advance for SENB specimen (load line displacement rate 0.15 mm s^{-1}).

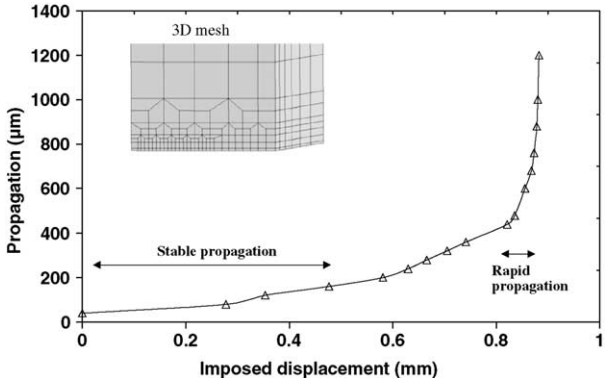

Fig. 10. Simulated crack advance for DENT $a/W = 0.1$ (load line displacement rate 0.15 mm s^{-1}).

ratio. Instability corresponds to a strong acceleration of the crack extension (arrow in Fig. 10). Due to the strain rate dependence of the material, stresses increase after the onset of instability. This is likely to lead to brittle failure as observed experimentally.

7. Conclusion

Viscoplastic and damage behavior of an unplasticized PVDF have been studied using different test geometries. Mechanical tests corroborated by fracture surface examinations and volume change measures indicate that damage is essentially caused by void growth. Softening by void growth and strain hardening by chain elongation occur simultaneously. A constitutive model accounting for both effects is employed to represent the mechanical behavior of the material. It is adjusted on tests carried out on smooth and notched tensile bars. It is validated on DENT and SENB specimens. The model reproduces well the observed instability on DENT specimens. Instability causes an increase of the strain rates and consequently of the stresses. This increase triggers brittle fracture.

References

[1] Prest WM, Luca DJ. The morphology and thermal response of high-temperature crystallized PVDF. J Appl Phys 1975;46(10):4136–43.
[2] Holstein P, Scheler U, Harris R. Semi crystallinity and polymorphism in PVDF: a solid state F NMR investigation. Polymer 1998;39(20):4937–41.
[3] Castagnet S, Girault S, Gacougnolle JL, Dang P. Cavitation in strained PVDF: mechanical and X-ray experimental studies. Polymer 2000;41(20):7523–30.
[4] Castagnet, S. Comportement mécanique du PVDF: Compétition entre cavitation et écoulement visqueux, Thesis, Poitiers, France, 1998 [in French].
[5] Hartmann B, Lee GF. Tensile yield in PCTFE and PVDF. Polym Eng Sci 1991;31:231–8.
[6] Gurson AL. Continuum theory of ductile rupture by void nucleation and growth: Part 1-yield criteria and flow rules for porous ductile media. J Eng Mater Technol 1977;99:2–15.
[7] Leevers PS. Impact and dynamic fracture of tough polymers by thermal decohesion in a dugdale zone. Int J Fract 1995;73:109–27.
[8] Gearing BP, Anand L. Notch sensitive fracture in polycarbonate. Int J Sol Struct 2004;41:827–45.
[9] Ivankovic A, Pandya KC, Williams JG. Crack growth predictions in PE using measured traction–separation curves. Engng Fract Mech 2004;71:657–68.
[10] Bridgman PW. Trans Am Soc Met 1944;32:553.

[11] Schultz JM. Microstructural aspects of failure in semicrystalline polymers. Polym Eng Sci 1984;24(10):770–85.
[12] Ishikawa M, Narisawa I, Ogawa H. Criterion for craze nucleation in polycarbonate. J Polym Sci 1977;15:1791–804.
[13] Narisawa I, Yee AF. Crazing and fracture of polymers. Mater Sci Technol. A comprehensive Treatment 1993;12:699–765.
[14] Hutchinson JW, Paris PC. Stability analysis of j-controlled crack growth. In: Landes JD, Begley JA, Clarke GA, editors. Elastic–plastic fracture, ASTM STP 668. American Society for Testing and Materials; 1979. p. 37–64.
[15] Paris PC, Tada H, Zahoor A, Ernst H. The theory of instability of the tearing mode of elastic-plastic crack growth. In: Landes JD, Begley JA, Clarke GA, editors. Elastic–plastic fracture, ASTM STP 668. American Society for Testing and Materials; 1979. p. 5–36.
[16] O'Dowd NP, Shih CF, Dodds RH. The role of geometry and crack growth on constraint and implications for ductile/brittle fracture. In: Kirk M, Bakker A, editors. Constraint effects in fracture: theory and applications. 1995. p. 134–59.
[17] Hertzberg RW, Manson JA, Skibo MD. Polym Eng Sci 1975;15:252.
[18] Thomasson PF. A theory for ductile fracture by internal necking of cavities. J Inst Metals 1968;96:360.
[19] Castagnet S, Gacougnolle JL, Dang P. Correlation between macroscopical viscoelastic behavior and micromechanisms in strained alpha PVDF. Mater Sci Eng 2000;A276:152–9.
[20] Quatravaux T, Elkoun S, G'Sell C, Cangemi L, Meimon Y. Experimental characterization of the volume strain of PVDF in the region of the homogeneous plastic deformation. J Polym Sci, Part B: Polym Phys 2002;40:2516–22.
[21] Tvergaard V. Influence of voids nucleation on ductile shear fracture at a free surface. J Mech Phys Solids 1982;30:399–425.
[22] Tvergaard V, Needleman A. Analysis of the cup-cone fracture in a round tensile bar. Acta Metall 1984;32:157–69.
[23] Besson J, Steglich D, Brocks W. Modeling of crack growth in round bars and plane strain specimen. Int J Sol Struct 2001:8259–84.
[24] Rousselier G. Ductile fracture models and their potential in local approach of fracture. Nucl Eng Des 1987;105:97–111.